Characterization of Zr-Doped TiO$_2$ Nanocrystals Prepared by a Nonhydrolytic Sol−Gel Method at High Temperatures

Sue-min Chang*,† and Ruey-an Doong‡

Institute of Environmental Engineering, National Chiao Tung University, 75, Po Ai Street, Hsinchu, 30068, Taiwan, and Department of Biomedical Engineering and Environmental Sciences, National Tsing Hua University, 101, Sec 2, Kuang Fu Road, Hsinchu, 30013, Taiwan

Highly crystalline and surface-modified Zr-doped TiO$_2$ nanorods were successfully prepared using a nonhydrolytic sol−gel method that involves the condensation of metal halides with alkoxides in anhydrous trioctylphosphine oxide (TOPO) at either 320 or 400 °C. In addition, the interaction of the cross-condensation between the Ti and Zr species was studied by characterizing the morphologies, crystalline structures, chemical compositions, surface properties, and band gaps of the nanocrystals obtained at different reaction temperatures and Zr-to-Ti stoichiometric ratios. Increases in the concentration of Zr^{4+} and in the reaction temperature led to large nanorods and regular shapes, respectively. In addition, only the anatase form was observed in the Zr-doped TiO$_2$ nanorods. The Zr-to-Ti ratios obtained ranged from 0.01 to 2.05, all of which were far below the stoichiometric ratios used during the preparation of the samples (0.25−4). Moreover, the Zr^{4+} units accumulated mainly at the surface of the TiO$_2$ nanocrystals. The band gaps of the Zr-doped TiO$_2$ nanorods ranged from 2.8 to 3.8 eV, which are smaller than those of pure TiO$_2$ (3.7 eV) or ZrO$_2$ (5.2 eV). The Zr-doped anatase TiO$_2$ nanorods prepared at 400 °C at an initial stoichiometric Zr-to-Ti ratio of 2:3 exhibited the highest photoactivities for the decomposition of rhodamine B because of the presence of trace amounts of Zr^{4+} (Zr/Ti = 0.03) in the TiO$_2$ and the regular shapes of these particles. DSC analysis indicated that the temperatures for forming nanocrystalline TiO$_2$ and ZrO$_2$ were 207 and 340 °C, respectively. Moreover, the reactivities of condensation between the Ti species were reduced when Zr species were involved in the NHSG reactions. The results obtained in this study clearly demonstrate that the faster kinetics for the generation of TiO$_2$ controls the material properties as well as the photoactivities of the nonhydrolytic sol−gel-derived nanocrystals.

Introduction

Titanium dioxide (TiO$_2$) is one of the most widely used photocatalysts because of its suitable band gap (ca. 3.2 eV), chemical stability, and nontoxicity.[1] In addition, zirconium dioxide (ZrO$_2$), which has a wide band gap (ca. 5.0 eV) and more-negative (−1.0 V vs NHE) and more-positive (4.0 V vs NHE) reducing potentials in its conduction and valence bands, respectively, relative to those of TiO$_2$, is considered as a promising alternative photocatalyst for the degradation of a greater variety of pollutants.[2−5] It has been demonstrated that incorporating Zr^{4+} into TiO$_2$ to form Zr$_x$Ti$_{1−x}$O$_2$ can introduce lattice defects and lead to higher photoactivities than those of the pure oxides. The introduced defects not only reduce the band gaps, i.e., increase the wavelength of the activation light, but also play a role as charge-trapping centers in inhibiting charge recombination.[6] Although the presence of a few defects improves the photoactivities of Zr$_x$Ti$_{1−x}$O$_2$ systems, an excess of defects promotes charge recombination and decreases catalytic efficiency. The number of defects is dependent on the size, crystalline structure, and Zr-to-Ti ratio of the photocatalyst.[7−9] Nanosize photocatalysts have large surface areas and sufficient numbers of surface defects to exhibit high catalytic efficiencies.

In addition, anatase TiO$_2$ and tetragonal ZrO$_2$ contain oxygen vacancies and exhibit higher catalytic performances than their other crystalline forms.[7,10−12] Therefore, the preparation and characterization of nanosize, highly crystalline anatase and tetragonal Zr$_x$Ti$_{1−x}$O$_2$ photocatalysts continues to attract a high degree of attention.

The sol−gel method is a simple and feasible process for the fabrication of nanocomposite oxides with tailored sizes. Conventionally, the sol−gel method uses a hydrolytic route that involves initial hydrolysis of the precursors and subsequent continuous condensation between the hydrolyzed precursors to form oxide gels. The hydrolytic sol−gel (HSG) route to metal oxides proceeds very efficiently at room temperature. In addition, nanoparticulates can be prepared through a combination of water-in-oil emulsion and sol−gel processing. Because the as-prepared oxides are usually amorphous, they must be calcined at high temperature for crystallization. Unfortunately, calcination results in the coalescence of particles, which increases the size and decreases the surface area of the photocatalysts.[13]

The nonhydrolytic sol−gel (NHSG) route is an alternative pathway for the preparation of metal oxides. In contrast to the HSG route, the NHSG route involves the reaction of metal halides with oxygen donors, such as metal alkoxides, alcohols, or ethers, under nonaqueous conditions.[14] Several studies have investigated the nonhydrolytic sol−gel route to pure oxides and binary oxides including TiO$_2$, ZrTiO$_4$, SiTiO$_4$, and SiZrO$_4$.[15−17]

* Corresponding author. E-mail: chang@mail.nctu.edu.tw. Tel.: +886-3-5712121 ext. 55506.
† National Chiao Tung University.
‡ National Tsing Hua University.

Characterization of Zr-Doped TiO$_2$ Nanocrystals

J. Phys. Chem. B, Vol. 110, No. 42, 2006 **20809**

Because the NHSG process is relatively slower than the HSG approach, it usually requires temperatures exceeding 80 °C. Moreover, the lower reactivity makes the morphologies and microstructures of NHSG-derived metal oxides more controllable. Trentler et al.[18] prepared anatase TiO$_2$ nanocrystals through the injection of titanium alkoxides into titanium isopropoxide/heptadecane solutions in the presence of trioctylphosphine oxide (TOPO) at 300 °C. These TiO$_2$ crystals had average sizes of 3.8−9.2 nm, depending on the type of the metal halide and the concentration of TOPO. Moreover, these TiO$_2$ nanoparticles exhibited no surface hydroxyl groups because of the coordination of the surface titanium atom to TOPO. Subsequently, Joo et al.[19] reported that condensation between zirconium halides and zirconium isopropoxide at 340 °C in pure TOPO results in monodisperse, uniformly sized tetragonal ZrO$_2$ nanoparticles (ca. 4 nm). In addition to pure metal oxides, binary metal oxides can also be prepared through cross-condensation between different metal halide and alkoxides. Tang et al.[20] adapted a process similar to that of Joo et al. to prepare monodisperse Hf$_x$Zr$_{1−x}$O$_2$ nanocrystals. Solid solutions with various concentrations were obtained after nonhydrolytic cross-condensations using different stoichiometric amounts of hafnium halides and zirconium alkoxides had been performed. In addition, the morphologies and crystalline phases within these solid solutions were controllable by modifying the reaction temperature and the combination of metal halide and alkoxide. Unfortunately, ZrTiO$_4$ solid solutions could not be formed using this method. This phenomenon is different from that of ZrTiO$_4$, for which the desired Zr-to-Ti ratios can be controlled by the initial metallic ratios in the solutions when the similar elimination of alkyl halides is conducted at low temperatures (110 °C).[17] In any event, the interaction between the Zr/Ti halides and alkoxides in the presence of TOPO at high temperatures has yet to be addressed adequately. In addition, the detailed quantification of the Zr-to-Ti ratios, microstructures, electronic structures, surface properties, and photoactivities of the Zr$_x$Ti$_{1−x}$O$_2$ nanocrystals resulting from various combinations of Zr and Ti species remain unclear.

In this study, we synthesized and characterized Zr-doped TiO$_2$ nanocrystals using an NHSG method conducted at 320 or 400 °C in liquid TOPO. Titanium chloride (TiCl$_4$) and zirconium chloride (ZrCl$_4$) were used as the precursors for TiO$_2$ and ZrO$_2$, respectively, and titanium isopropoxide and zirconium isopropoxide were used as the oxygen donors. To understand explicitly the chemistry of the cross-condensation leading to the Zr-doped TiO$_2$ nanocrystals, we examined the material properties—including particle sizes, shapes, crystalline phases, surface compositions, surface properties, and optical properties—of the products prepared at various stoichiometric Zr-to-Ti ratios and reaction temperatures. Moreover, we investigated the photocatalytic activities of the Zr-doped TiO$_2$ samples toward the degradation of rhodamine B (RhB) and elucidated how they relate to the material properties.

Experimental Section

NHSG-Derived Nanocrystals. Titanium dioxide (TiO$_2$) nanocrystals were prepared by condensation between titanium chloride (TiCl$_4$, Fluka, 99%) and Ti(OC$_3$H$_7$)$_4$ (Aldrich, 99.9%), whereas zirconium dioxide (ZrO$_2$) nanocrystals were fabricated by zirconium chloride (ZrCl$_4$, Strem Chemicals, 99.5%) and zirconium isopropoxide propanol complex [Zr(OC$_3$H$_7$)$_4$−(CH$_3$)$_2$CHOH, Aldrich, 99.9%]. Titanium chloride (0.5 g, 2.5 mmol) and Ti(OC$_3$H$_7$)$_4$ (0.6 g, 2.0 mmol) were first dissolved in TOPO (5.2 g, 13.5 mmol) at 150 °C under N$_2$ atmosphere. This well-

TABLE 1: Metal Halides, Oxygen Donors, and Reaction Temperatures Used for the Synthesis of Zr$_x$Ti$_{1−x}$O$_2$ Nanoparticles

sample	metal halide (2.5 mmol)	oxygen donor(s)	TOPO (mmol)	temp (°C)
TiO$_2$-320	TiCl$_4$	Ti(OC$_3$H$_7$)$_4$ (2.0 mmol)	13.5	320
Zr$_{0.2}$Ti$_{0.8}$O$_2$-320	TiCl$_4$	Ti(OC$_3$H$_7$)$_4$ (1.0 mmol), Zr(OC$_3$H$_7$)$_4$·(CH$_3$)$_2$CHOH (1.0 mmol)	13.5	320
Zr$_{0.4}$Ti$_{0.6}$O$_2$-320	TiCl$_4$	Zr(OC$_3$H$_7$)$_4$·(CH$_3$)$_2$CHOH (2.0 mmol)	13.5	320
Zr$_{0.2}$Ti$_{0.8}$O$_2$-400	TiCl$_4$	Ti(OC$_3$H$_7$)$_4$ (1.0 mmol), Zr(OC$_3$H$_7$)$_4$·(CH$_3$)$_2$CHOH (1.0 mmol)	13.5	400
Zr$_{0.4}$Ti$_{0.6}$O$_2$-400	TiCl$_4$	Zr(OC$_3$H$_7$)$_4$·(CH$_3$)$_2$CHOH (2.0 mmol)	13.5	400
Zr$_{0.6}$Ti$_{0.4}$O$_2$-400	ZrCl$_4$	Ti(OC$_3$H$_7$)$_4$ (2.0 mmol)	21	400
Zr$_{0.8}$Ti$_{0.2}$O$_2$-400	ZrCl$_4$	Ti(OC$_3$H$_7$)$_4$ (1.0 mmol), Zr(OC$_3$H$_7$)$_4$·(CH$_3$)$_2$CHOH (1.0 mmol)	21	400
ZrO$_2$-400	ZrCl$_4$	Zr(OC$_3$H$_7$)$_4$·(CH$_3$)$_2$CHOH (2.0 mmol)	21	400

mixed solution was then heated to 320 °C and underwent the condensation reaction at this temperature for 3 h with vigorous stirring at 500 rpm. Afterward, the solution was cooled to 60 °C, and acetone was added to precipitate TiO$_2$ nanocrystals. The precipitate was harvested by centrifugation at 11000 rpm and washed with acetone several times to remove excess TOPO. For ZrO$_2$ preparation, 0.6 g of ZrCl$_4$ (2.5 mmol) and 0.8 g of Zr(OC$_3$H$_7$)$_4$−(CH$_3$)$_2$CHOH (2.0 mmol) were dissolved in 8.0 g of TOPO (21 mmol). The ratio of metal chloride to alkoxide is similar to that used by Joo et al.,[19] which means that the metal chloride was in excess. In contrast to TiO$_2$, ZrO$_2$ particles were produced only when the temperature rose to 400 °C. For the synthesis of Zr-doped TiO$_2$ nanocrystals, various molar ratios of M(O^{i}Pr)$_4$ and M′Cl$_4$ (M and M′ represent Ti and/or Zr) were used. The samples are denoted as Zr$_x$Ti$_{1−x}$O$_2$-t, where x represents the reactants in the ratio of Zr/(Zr + Ti) and t denotes the reaction temperature. The nonhydrolytic reaction was carried out at 320 or 400 °C when x was smaller than 0.5 and 400 °C for x larger than 0.5. All recipes and reaction conditions are summarized in Table 1. Unless otherwise mentioned, all of the NHSG reactions were conducted in hot trioctylphosphine oxide (TOPO, Strem Chemicals, 99%) liquid and under N$_2$ atmosphere.

Characterization. The thermal behaviors of the NHSG reactions were investigated by differential scanning calorimetry (DSC, Setaram Labsys DSC 131) under a N$_2$ flow of 20 mL/min and at a heating rate of 10 °C/min from 25 to 550 °C. The samples for DSC were prepared by dissolving the reactants in TOPO at 150 °C and then cooling the mixture to room temperature under N$_2$ atmosphere. The TiCl$_4$/Ti(O^{i}Pr)$_4$/TOPO mixture was a viscous yellow liquid, and the ZrCl$_4$/Zr(O^{i}Pr)$_4$/TOPO mixture was an opaque white solid. The particle sizes and shapes of the NHSG-derived nanocrystals were characterized by high-resolution transmission electron microscopy (HRTEM, JEOL JEM-4000EX) at an accelerating voltage of 400 kV. The crystalline properties of the nanocrystals were identified by X-ray diffractometry (XRD, Rigaku) using Cu Kα radiation (λ = 1.5405 Å) and operating at an accelerating voltage of 30 kV and an emission current of 20 mA. The X-ray diffraction patterns

20810 *J. Phys. Chem. B, Vol. 110, No. 42, 2006*

Chang and Doong

were acquired over the 2θ range from 20° to 90° at a sampling width of 0.02° and a scanning speed of 4°/min. The elemental compositions (Zr/Ti) of the binary metal oxides were analyzed by inductively coupled plasma−mass spectrometry (ICP-MS, Perkin-Elmer, SCIEX ELAN 5000). The surface chemical compositions of the nanocrystals were examined by X-ray photoelectron spectroscopy (XPS, Physical Electronics, ESCA PHI 1600) using an Al Kα X-ray source (1486.6 eV). The photoelectrons were collected into the analyzer with a 23.5 eV passing energy. The collection step was 1.0 eV for the wide-range scan and 0.1 eV for high-resolution analysis in selected energy intervals. All analytical processes were carried out under ultrahigh vacuum conditions with the pressure maintained below 1.4×10^{-9} Torr. The shifts of the photoelectron peaks in the XPS spectra resulting from charging effects were referenced to the O(1s) line taken as 530.2 eV. The surface elemental ratios were estimated from the integrated peak areas of the elements and normalized to their sensitivity factors. The functional groups of the nanoparticles were identified by Fourier transform infrared spectrometry (FTIR, Horiba) scanning from 400 to 4000 cm^{-1} with a resolution of 4 cm^{-1} for 100 scans. Samples for FTIR measurements were well-mixed with KBr and then pressed as pellets. The optical properties and band gaps of the nanoparticles were determined by UV−vis spectrophotometry (Hitachi 3010) scanning from 800 to 190 nm using the absorption of hexane as the reference. Samples for the UV−vis measurements were well-dispersed in hexane in a quartz cuvette with an optical length of 10 mm.

Photocatalytic Activities. Rhodamine B (RhB) was selected as the target compound to examine the photoactivity of the NHSG-derived $Zr_xTi_{1-x}O_2$ materials. The nanocrystalline catalysts were suspended in RhB solutions (0.05 mM) to give a final concentration of 1 g/L in the dark. Prior to illumination, the solutions were purged with O_2 in the dark for 30 min to ensure equilibrium among the catalysts, RhB, and oxygen. Thereafter, the solutions were kept under constant O_2 equilibrium condition during photocatalysis. Photocatalysis was carried out in a fused-silica tube irradiated by UV light at a wavelength of 305 nm. The decolored solutions were analyzed by UV−vis spectrophotometer scanning from 700 to 400 nm.

Results and Discussion

Chemical Compositions. To examine the chemical states of the Ti and Zr species after the nonhydrolytic sol−gel reaction, the NHSG-derived samples were analyzed using XPS (see Supporting Information, Figure S1). The binding energy of Zr(3d$_{5/2}$) centered at 182.3 eV in the ZrO_2 spectrum, and that of Ti(2p$_{3/2}$) was at 459.0 eV in the TiO_2 spectrum. Similarly to pure TiO_2 and ZrO_2, Zr(3d$_{5/2}$) and Ti(2p$_{3/2}$) in $Zr_xTi_{1-x}O_2$ nanocrystals exhibited binding energies in the ranges 182.3−182.5 and 458.7−459.0 eV, respectively. These values are in good agreement with the reported values for TiO_2, ZrO_2, and $ZrTiO_4$,[21] which indicates the formation of Ti−O and Zr−O bonds in the samples via the nonhydrolytic reactions. Table 2 lists the actual Zr-to-Ti ratios of the $Zr_xTi_{1-x}O_2$ nanocrystals as analyzed using both ICP-MS and XPS. The Zr-to-Ti ratios of the binary oxides determined by ICP-MS ranged from 0.01 to 2.05, whereas a range of 0.02−2.29 was obtained through XPS analysis. It is noted that ICP-MS is an instrumental method that can determine the total concentrations of elements in $Zr_xTi_{1-x}O_2$ nanocrystals suspended in solution, whereas XPS is usually employed for the analysis of chemical species on the surfaces of nanocrystals. The similar Zr-to-Ti ratios obtained in these two methods reveal that most of the Zr^{4+} ions accumulated in
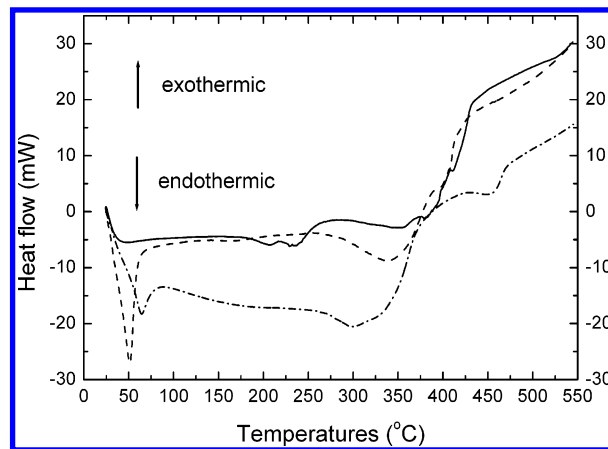

Figure 1. DSC curves of the NHSG reactions leading to TiO_2 (solid line), ZrO_2 (dashed line), and $Zr_{0.25}Ti_{0.75}O_2$ (dashed−dotted line) in the presence of TOPO.

TABLE 2: Zr-to-Ti Molar Ratios and Actual Compositions of the Binary Oxide Nanoparticles

$Zr_xTi_{1-x}O_2$ nanocrystals	Zr-to-Ti molar ratio[a]		
	ICP-MS	XPS	actual composition
$Zr_{0.2}Ti_{0.8}O_2$-320	0.03	b	$Zr_{0.03}Ti_{0.97}O_2$-320
$Zr_{0.4}Ti_{0.6}O_2$-320	0.05	0.02	$Zr_{0.05}Ti_{0.95}O_2$-320
$Zr_{0.2}Ti_{0.8}O_2$-400	0.01	b	$Zr_{0.01}Ti_{0.99}O_2$-400
$Zr_{0.4}Ti_{0.6}O_2$-400	0.03	0.05	$Zr_{0.03}Ti_{0.97}O_2$-400
$Zr_{0.6}Ti_{0.4}O_2$-400	0.34	0.33	$Zr_{0.25}Ti_{0.75}O_2$-400
$Zr_{0.8}Ti_{0.2}O_2$-400	2.05	2.29	$Zr_{0.67}Ti_{0.33}O_2$-400

[a] Molar ratios were determined by ICP-MS and XPS. [b] Detection of Zr was not possible.

the surface layer of the nanocrystals. When the value of x was greater than 0.5, the actual Zr-to-Ti ratios in the nanocrystals increased with increasing content of Zr in the reaction mixture. No such trend occurred, however, when the value of x was below 0.5. The similar Zr-to-Ti ratios (0.01−0.05) in the $Zr_{0.2}$-$Ti_{0.8}O_2$ and $Zr_{0.4}Ti_{0.6}O_2$ samples prepared at 320 and 400 °C indicate that increasing temperature had little effect on the degree of incorporation of Zr into the TiO_2 lattice.

Regardless of the initial Zr-to-Ti ratio used for the synthesis of the binary oxides, the final Zr-to-Ti ratios in the products were always much smaller than the theoretical stoichiometry. This phenomenon is attributed to the different kinetics of condensation between Ti and Zr species. Actually, the formation of TiO_2 through the condensation of $TiCl_4$ with $Ti(OC_3H_7)_4$ occurs at 320 °C, but a higher temperature (400 °C) is required for the preparation of ZrO_2. Because the actual compositions of $Zr_xTi_{1-x}O_2$ are different from the stoichiometric values, we use the actual ratios based on ICP-MS results for further discussion.

Heat Flows during NHSG Reactions. To understand the different dynamic properties of the NHSG reactions that form TiO_2, ZrO_2, and $Zr_xTi_{1-x}O_2$, we used DSC to examine the heat flows of these reactions. Figure 1 displays the heat flows of the NHSG reactions forming TiO_2, ZrO_2, and $Zr_{0.25}Ti_{0.75}O_2$-400 in the presence of TOPO. The NHSG reaction leading to TiO_2 exhibited two endothermic peaks in the temperature range from 180 to 270 °C. The endothermic peak centered at 207 °C is ascribed to the condensation between ≡Ti−Cl and ≡Ti−(OC$_3$H$_7$), and the peak ranging between 218 and 270 °C is attributed to the halide/titanyl exchange. This exchange results in the breaking and reforming of Ti−O bonds, which is considered to be necessary for the crystallization of TiO_2.[18] The DSC trace for the NHSG reaction leading to ZrO_2 exhibited two

Characterization of Zr-Doped TiO$_2$ Nanocrystals

J. Phys. Chem. B, Vol. 110, No. 42, 2006 **20811**

significant endothermic peaks centered at 51 and 340 °C, which are attributed to the liquefaction of the ZrCl$_4$/Zr(O^{i}Pr)$_4$/TOPO complex and the condensation of ≡Zr—Cl with ≡Zr—(OC$_3$H$_7$), respectively. The DSC results clearly indicate that the temperatures for the formation of TiO$_2$ nanocrystals (207 °C) are lower than those required for the generation of NHSG-derived ZrO$_2$ (340 °C), which means the the condensation reactivity of Ti species is higher than that of Zr species.

To understand the interaction between the Ti and Zr species, the DSC curve of Zr$_{0.25}$Ti$_{0.75}$O$_2$ was further examined. Similarly to ZrO$_2$, Zr$_{0.25}$Ti$_{0.75}$O$_2$ exhibited endothermic melting of the TOPO complex at 65 °C. However, the endothermic melting process was not obvious in the DSC curve of TiO$_2$. This is mainly attributed to the fact that TiCl$_4$/Ti(O^{i}Pr)$_4$/TOPO mixture is a viscous liquid, whereas the ZrCl$_4$/Zr(O^{i}Pr)$_4$/TOPO and ZrCl$_4$/Ti(O^{i}Pr)$_4$/TOPO mixtures are solids at room temperature. The Zr$_{0.25}$Ti$_{0.75}$O$_2$ sample exhibited an endothermic peak of condensation centered at 300 °C. Because the elemental analysis showed that TiO$_2$ is the dominant component in Zr$_{0.25}$Ti$_{0.75}$O$_2$, this condensation mainly occurs between ≡Ti—Cl and ≡Ti—(O^{i}Pr), which result from ligand exchange between ≡Ti—(O^i-Pr) and ≡Zr—Cl at low temperatures. Ligand exchange between metal chlorides and metal alkoxides has been demonstrated to produce metal chloroalkoxides, and thus homogeneous as well as heterogeneous condensations can occur.[17] It is noted that the temperature for condensation between the Ti species for Zr$_{0.25}$-Ti$_{0.75}$O$_2$ (300 °C) was higher than that for TiO$_2$ (207 °C), which suggests that the Ti species in the Zr$_{0.25}$Ti$_{0.75}$O$_2$ precursor solution is different from that in the TiO$_2$ precursor solution. Arnal et al.[16] reported that metal chloroalkoxides are present in oligomeric structures because of the formation of alkoxo bridges. In this study, titanium zirconium chloroalkoxide oligomers could be produced in the Zr$_{0.25}$Ti$_{0.75}$O$_2$ precursor solution after ligand exchange. Compared to the pure titanium chloroalkoxide isomers, the Ti species have a lower reactivity to condense with each other to form Ti—O—Ti bonds when Zr species coexist with Ti species.

The endothermic peak for Zr$_{0.25}$Ti$_{0.75}$O$_2$ appearing at 334 °C in the DCS curve can be assigned to the formation of Zr—O—Ti bonds through cross-condensation. This cross-condensation is responsible for the incorporation of Zr into the TiO$_2$ lattice. However, the low Zr-to-Ti ratios reveal that the formation of Zr$_x$Ti$_{1-x}$O$_2$ nanocrystals is kinetically controlled because the temperature required for the formation of TiO$_2$ is lower than that for the formation of binary oxides. The relatively rapid formation of TiO$_2$ nanocrystals results in the inefficient condensation of Zr species during a dynamic equilibrium. The Zr components were lost either because the reaction temperature (320 °C) was too low to form ZrO$_2$ or because the ZrO$_2$ particles that formed were too small to be recovered through centrifugation at 11000 rpm at 400 °C. In contrast to the ineffective incorporation of Zr into TiO$_2$ in this study, Vioux et al.[17] reported that amorphous zirconium titanate gels with Zr-to-Ti ratios equal to those of the initial solutions were obtained using a similar cross-condensation process at 110 °C. In addition, the temperature of condensation between Ti—Cl and Ti—O^{i}Pr was reported to be 100 °C,[16] which is lower than the temperature for the condensation of pure TiO$_2$ (207 °C) obtained in this study. This discrepancy is due to the fact that TOPO modifies the thermodynamic properties and kinetics of the nonhydrolytic sol−gel reactions by forming Lewis adducts with the precursors.

Microstructures. To identify the effect of the preparation conditions on the microstructures of Zr-doped TiO$_2$, the NHSG-derived Zr$_x$Ti$_{1-x}$O$_2$ samples were further analyzed using HR-
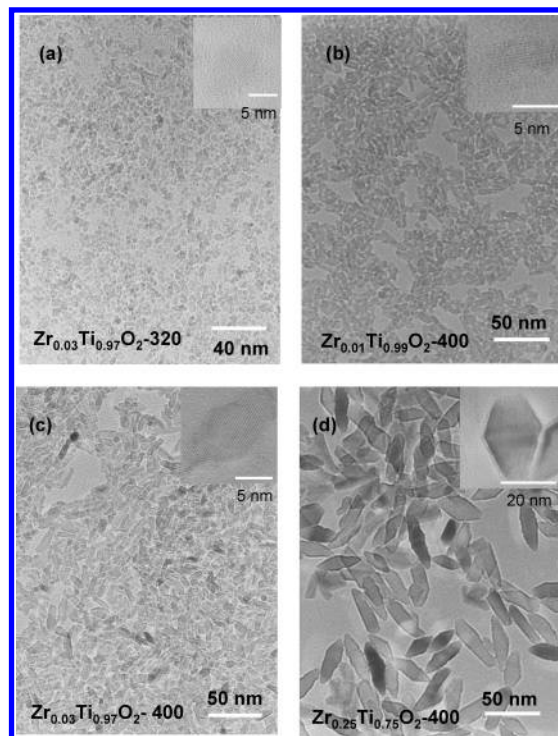

Figure 2. HRTEM images of NHSG-derived nanocrystals: (a) Zr$_{0.03}$-Ti$_{0.97}$O$_2$-320, (b) Zr$_{0.01}$Ti$_{0.99}$O$_2$-400, (c) Zr$_{0.03}$Ti$_{0.97}$O$_2$-400, (d) Zr$_{0.25}$-Ti$_{0.75}$O$_2$-400.

TEM and XRD. Figure 2 shows HRTEM images of Zr$_{0.03}$-Ti$_{0.97}$O$_2$-320, Zr$_{0.01}$Ti$_{0.99}$O$_2$-400, Zr$_{0.03}$Ti$_{0.97}$O$_2$-400, and Zr$_{0.25}$-Ti$_{0.75}$O$_2$-400 nanocrystals. The HRTEM images indicate that the NHSG-derived TiO$_2$ and ZrO$_2$ nanocrystals were almost spherical, except for a few that have irregular shapes as a result of aggregation (see Supporting Information, Figure S2). The sizes of the TiO$_2$ and ZrO$_2$ particles, as observed from low-magnification TEM images, were ca. 4.5 and 3.0 nm, respectively. Highly crystalline structures and single crystallinity were observed for both the TiO$_2$ and ZrO$_2$ particles in high-magnification TEM images. Because TOPO plays the role of a capping agent that isolates the NHSG-derived nanocrystals, these relatively small ZrO$_2$ nanocrystals arose from the lower metal-to-TOPO ratio that we used in these NHSG reactions.

The Zr$_{0.03}$Ti$_{0.97}$O$_2$ nanocrystals prepared at 320 °C exhibited irregular shapes and a wide size distribution. A similar phenomenon was also observed for Zr$_{0.05}$Ti$_{0.95}$O$_2$-320 (see Supporting Information, Figure S2). The sizes and shapes became more uniform when the reaction temperature rose to 400 °C. The Zr$_{0.03}$Ti$_{0.97}$O$_2$-400 and Zr$_{0.25}$Ti$_{0.75}$O$_2$-400 nanoparticles became faceted nanorods at 400 °C (Figure 2c,d). The lengths and widths of the Zr$_{0.03}$Ti$_{0.97}$O$_2$-400 nanorods were of ca. 15.0 and 8.0 nm, respectively, whereas the corresponding dimensions of the Zr$_{0.25}$-Ti$_{0.75}$O$_2$-400 nanorods were ca. 30.0 and 14.0 nm, respectively. The high-magnification HRTEM images showed that the nanorods existed in a single crystalline domain but contained a considerable number of defects on their edges. In addition, the Zr$_{0.25}$Ti$_{0.75}$O$_2$-400 nanorods were covered with a thin layer of amorphous material. A similar amorphous structure was dominant in the Zr$_{0.67}$Ti$_{0.33}$O$_2$-400 sample.

Figure 3 displays the XRD patterns of TiO$_2$, ZrO$_2$, and Zr$_x$Ti$_{1-x}$O$_2$ samples with various values of *x*. The TiO$_2$ and ZrO$_2$ particles obtained crystallized in the anatase and tetragonal forms, respectively, without further calcination. In addition, the Zr$_{0.03}$Ti$_{0.97}$O$_2$-320, Zr$_{0.05}$Ti$_{0.95}$O$_2$-320, Zr$_{0.01}$Ti$_{0.99}$O$_2$-400, Zr$_{0.03}$-Ti$_{0.97}$O$_2$-400, and Zr$_{0.25}$Ti$_{0.75}$O$_2$-400 samples exhibited only

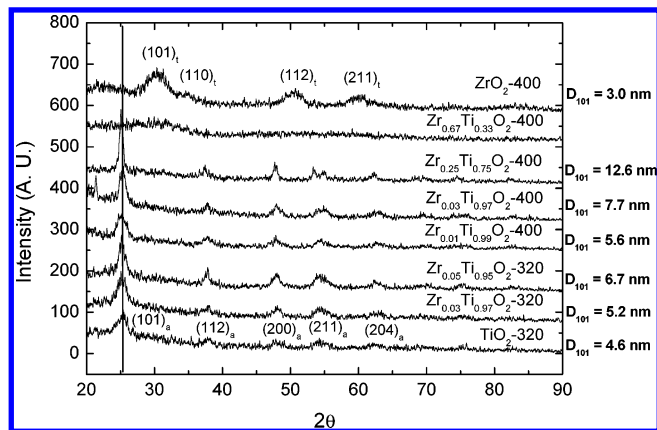**Figure 3.** XRD patterns of TiO_2, ZrO_2, and $Zr_xTi_{1-x}O_2$ nanocrystals.

anatase structures, and no ZrO_2 or $ZrTiO_4$ diffraction peaks were identified, even though substantial amounts of Zr reactants had been added to participate in the nonhydrolytic reactions. This result is mainly due to the fact that the Zr^{4+} ions serve only as dopants in the TiO_2 matrix. Moreover, the diffraction peak of the $(101)_a$ profile of $Zr_{0.25}Ti_{0.75}O_2$-400 shifted slightly to a lower value of 2θ when compared to that of the pure TiO_2 nanocrystals, revealing that the Zr^{4+} ions, with a larger ionic radius (0.79 Å) than Ti^{4+} (0.68 Å), were incorporated into the TiO_2 lattice to form dilute $Zr_xTi_{1-x}O_2$ solid solutions. The XRD results show the poor crystallinity of the $Zr_{0.67}Ti_{0.33}O_2$-400 sample, which is in agreement with the observation of the amorphous structure in its HRTEM image. The Zr-to-Ti ratio of 2.05 in the $Zr_{0.67}Ti_{0.33}O_2$-400 sample clearly indicates that substantial amounts of TiO_2 are present in the ZrO_2 matrix. These results suggest that higher temperatures are required for crystallization of the binary oxide solutions than for crystallization of pure TiO_2 and ZrO_2 in the nonhydrolytic sol−gel reactions. Vioux et al.[17] found that an NHSG-derived $ZrTiO_4$ sample crystallized at 700 °C. The high temperatures required for crystallized $Zr_xTi_{1-x}O_2$ solid solutions at high Zr concentrations probably arise because the anatase TiO_2 and tetragonal ZrO_2 structures are not compatible with each other. The anatase $Zr_{0.25}Ti_{0.75}O_2$-400 nanocrystals contained amorphous structures at their edges. It has been previously demonstrated that the solubility of Zr^{4+} units in sol−gel-derived anatase TiO_2 is below the Zr-to-Ti ratio of 0.075.[22] The excess Zr^{4+} ions (i.e., 0.34 > 0.075) in the $Zr_{0.25}Ti_{0.75}O_2$-400 sample would primarily accumulate at the surface of the anatase TiO_2 nanocrystals because of slow condensation involving the Zr species and segregation of the Zr^{4+} ions to maintain phase stability. Therefore, the amorphous material at the edges of the $Zr_{0.25}Ti_{0.75}O_2$-400 nanorods presumably comprises cross-linked Zr and Ti binary oxides that are unable to crystallize in this nonhydrolytic sol−gel reaction.

The average crystallite sizes of anatase TiO_2 and tetragonal ZrO_2, calculated using Scherrer's equation from the broadening of diffraction peaks of the $(101)_a$ and $(101)_t$ profiles, were 4.6 and 3.0 nm, respectively. These values are close to the particle sizes observed in the TEM images. Because of the single crystallinity of the NHSG-derived nanocrystals, the size distributions and variations were examined from the TEM images. The TiO_2 and ZrO_2 nanoparticle sizes have uncertainties of ±1.0 and ±0.9 nm, respectively. The crystallite sizes of the $Zr_{0.03}Ti_{0.97}O_2$-320 and $Zr_{0.05}Ti_{0.95}O_2$-320 samples were 5.2 ± 1.4 and 6.7 ± 2.5 nm, respectively; i.e., an increased Zr-to-Ti ratio increased the crystallite sizes. In addition, both the crystallite sizes and the size distributions of the $Zr_{0.01}Ti_{0.99}O_2$-400 (5.6 ± 1.0 nm) and $Zr_{0.03}Ti_{0.97}O_2$-400 (7.7 ± 1.9 nm) samples were larger than those obtained at 320 °C, indicating that increasing

reaction temperature makes the crystallite sizes larger and more uniform. The $Zr_{0.25}Ti_{0.75}O_2$-400 sample exhibited the largest crystallite size of 12.6 ± 2.5 nm because it was prepared at a high Zr-to-Ti ratio and reaction temperature.

The TEM observations and XRD results reveal that the initial Zr-to-Ti ratio and reaction temperature affect the sizes and shapes of the NHSG-derived $Zr_xTi_{1-x}O_2$ nanocrystals. The initial Zr-to-Ti ratio affects the morphology of the $Zr_xTi_{1-x}O_2$ samples by affecting the condensation rate. It has been suggested that the rate of alkyl halide elimination governs the nucleation and growth of nanocrystals.[18] In this study, because the presence of Zr species retarded the formation of TiO_2, the sizes of the nanocrystals increased as the Zr-to-Ti ratio increased. In addition to the crystallite sizes, the different reactivities between Ti and Zr species also play the crucial role in the shapes and size distributions of the NHSG-derived nanocrystals. At 320 °C, the growth of TiO_2 nanocrystals is inhibited at the end where the Ti species are hybridized with less-reactive Zr species, thus resulting in the irregular shape of Zr-doped TiO_2. However, this low reactivity can be kinetically promoted by increasing the reaction temperature. Trentler et al.[18] suggested that the formation and breaking of Ti—O bonds at elevated temperatures helps to erase the defects and, hence, result in more-crystalline structures. In this study, increasing temperature encourages the rearrangement of Ti and O atoms, leading to the elimination of the defects caused by Zr^{4+} and the formation of regularly shaped nanocrystals. This phenomenon was not observed when a similar reaction protocol was used for the preparation of $Hf_xZr_{1-x}O_2$ nanoparticles.[20] This discrepancy might be due to the fact that Zr and Hf species have similar reactivities, whereas the Ti species have a higher reactivity than the Zr species in the nonhydrolytic sol−gel reactions.

Surface Properties. In contrast to the hydrophilic surfaces of the metal oxides obtained using the conventional HSG method, the surfaces of the metal oxides obtained in this study were hydrophobic. The nanocrystals were readily soluble in hexane, but they were difficult to suspend in water. The XPS results indicate the existence of substantial amounts of carbon and small amounts of phosphorus on the surfaces of the nanocrystals, suggesting that some TOPO residues existed on the surface of the metal oxides (see Supporting Information, Figure S3). The C-to-P molar ratio ranged between 18 and 20, which is lower than that expected for TOPO (C/P = 24). In addition, the O^*-to-P ratios (where O^* denotes oxygen atoms other than M—O atoms) were in the range 2−3, which is larger than the intrinsic value (O/P = 1) expected for TOPO (see Supporting Information, Table 1S). These results imply that the TOPO molecules were decomposed during the high-temperature reactions. To investigate the interactions between TOPO and the nanocrystals, we used FTIR spectroscopy to further characterize the functional groups present on the surfaces of the nanocrystals. Figure 4 displays the FTIR spectra of TOPO, the as-prepared nanocrystals, and the nanocrystals obtained after photocatalysis. The spectrum of TOPO exhibited a significant absorption at 1146 cm^{-1} that was due to P=O stretching. The corresponding most intense absorptions for the TiO_2 and ZrO_2 nanocrystals appeared at 1065 cm^{-1}. The shift from 1146 to 1065 cm^{-1} indicates that the P=O groups were chelated to the surface Zr^{4+} or Ti^{4+} centers. Figure 5 presents a cartoon illustration of the surface structure of an NHSG-derived nanocrystal based on the XPS and FTIR spectroscopic data. The surfaces of the nanocrystals are covered by TOPO units, which are chemically bonded to the surface through chelation of the P=O oxygen atoms or through defunctionalization of the P=O groups

Characterization of Zr-Doped TiO₂ Nanocrystals

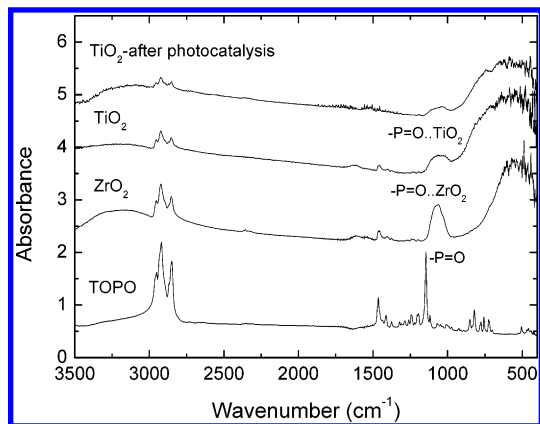*J. Phys. Chem. B, Vol. 110, No. 42, 2006* **20813**

Figure 4. FTIR spectra of pure TOPO and TOPO-capped ZrO₂ and TiO₂ nanocrystals, the latter recorded before and after photocatalysis.
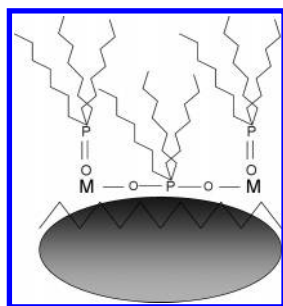

Figure 5. Surface chemical structures of NHSG-derived nanocrystals.

to form new P—O—M bonds. After photocatalysis, the intensity of the signal for TOPO decreased, implying that a certain amount of TOPO decomposed during photocatalysis. The P-to-Ti and C-to-P elemental ratios of the NHSG-derived TiO₂ before and after photocatalysis were further analyzed by XPS. The P-to-Ti ratio remained at a similar value (2.01), whereas the C-to-P ratio decreased from 19.1 to 11.1 after photocatalysis. These XPS and IR results reveal that photocatalysis causes the decomposition of the surface TOPO through the removal of organic parts and the transformation of P=O functional groups to other phosphorus species.

Optical Properties. The band gaps and quantum effects on the optical properties of the nanocrystals were determined by UV−vis spectrophotometry. Figure 6 presents the UV−vis spectra of the TiO_2, ZO_2, and $Zr_xTi_{1-x}O_2$ nanocrystals suspended in hexane. The TiO₂ nanocrystals showed a steep increase in their absorptions at wavelengths below 333 nm, and the ZrO₂ nanocrystals exhibited significant absorptions at wavelengths below 234 nm. The band gaps of the pure TiO₂ and ZrO₂ nanocrystals, derived from the onsets of these significant absorptions, were 3.7 and 5.3 eV, respectively, which are larger than those of bulk TiO₂ (3.2 eV) and ZrO₂ (5.0 eV).[1,23] This phenomenon indicates that quantum effects occurred and that the nanocrystals obtained were quantum-sized. The anatase Zr-doped TiO₂ crystals exhibited absorptions that extended to longer wavelengths. The band gaps of the Zr-doped TiO₂ crystals ranged between 2.8 and 3.6 eV, i.e., they were smaller than those of pure TiO₂ or ZrO₂ nanocrystals. Presumably, these red shifts and reduced band gaps resulted either from defects caused by trace amounts of Zr^{4+} in the TiO₂ lattice or from increased crystal domains. We note that the $Zr_{0.25}Ti_{0.75}O_2$-400 sample exhibited marked absorptions up to 600 nm. This extrinsic band gap absorption of $Zr_{0.25}Ti_{0.75}O_2$-400 is attributed to the accumulation of substantial amounts of Zr^{4+} at the surface of the TiO₂ anatase crystals. A similar effect occurred for amorphous $Zr_{0.67}Ti_{0.33}O_2$-400, which contained mainly ZrO₂
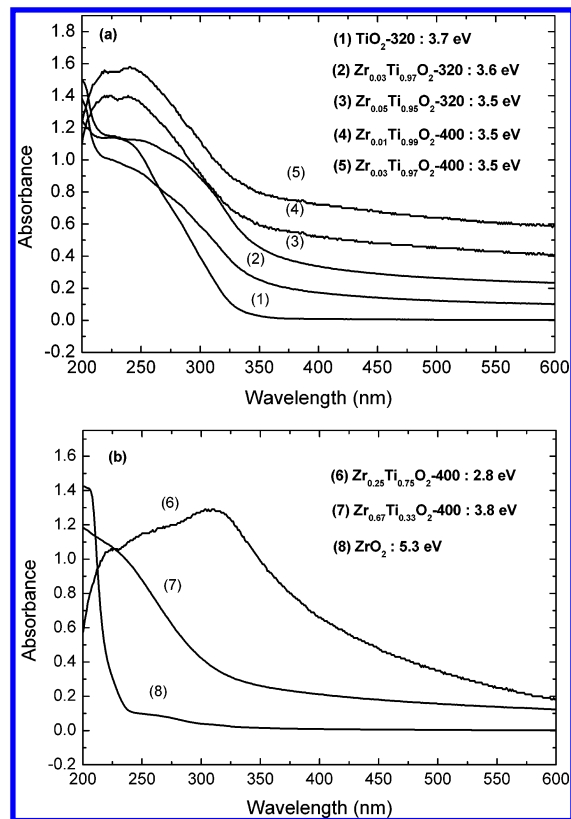

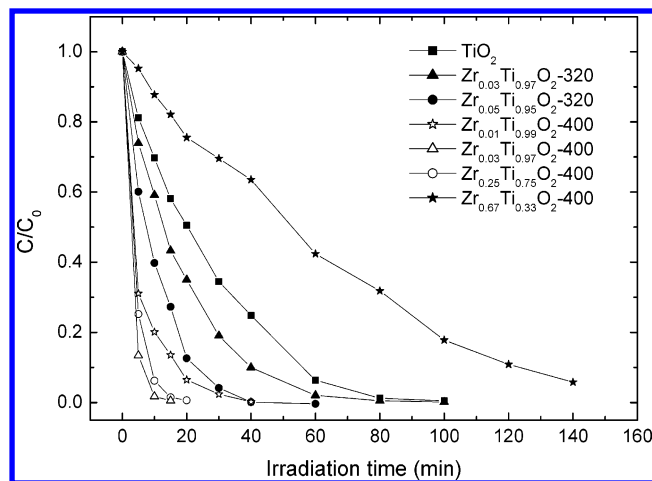**Figure 6.** UV−vis spectra of NHSG-derived nanocrystals.

Figure 7. Photodegradation of RhB in the presence of NHSG-derived nanocrystals.

with TiO₂ in a comparative amount (Zr/Ti = 2.1) and exhibited a band gap of 3.8 eV. Large amounts of Ti^{4+} in the ZrO₂ matrix not only inhibited the crystallization of ZrO₂ but also greatly reduced the band gap of ZrO₂ from 5.3 to 3.8 eV.

Photoactivities of the NHSG-Derived Nanocrystals. We examined the photoactivities of the NHSG-derived nanocrystals by considering the decoloration of RhB monitored at 554 nm. Figure 7 shows the change in RhB concentration as a function of irradiation time. In the absence of a photocatalyst, RhB was stable when illuminated with UV light at 305 nm. The rapid degradation of RhB in the presence of the prepared nanocrystals indicates that each of the TOPO-capped photocatalysts exhibited photoactivity. Although the band transitions of ZrO₂ nanocrystals occur below 234 nm, electron transitions between the defect levels and bands result in the ZrO₂ nanocrystals having photocatalytic functions at 305 nm. The photodecomposition of RhB

followed pseudo-first-order kinetics. The $Zr_{0.03}Ti_{0.97}O_2$-400 sample ($k = 0.40$ min^{-1}) exhibited the highest rate of decomposition of RhB, followed by $Zr_{0.25}Ti_{0.75}O_2$-400 ($k = 0.28$ min^{-1}), $Zr_{0.01}Ti_{0.99}O_2$-400 ($k = 0.13$ min^{-1}), $Zr_{0.05}Ti_{0.95}O_2$-320 ($k = 0.10$ min^{-1}), $Zr_{0.03}Ti_{0.97}O_2$-320 ($k = 0.07$ min^{-1}), TiO_2-320 ($k = 0.04$ min^{-1}), $Zr_{067}Ti_{0.33}O_2$-400 ($k = 0.01$ min^{-1}), and then ZrO_2 ($k = 3.2 \times 10^{-3}$ min^{-1}).

The $Zr_xTi_{1-x}O_2$ nanocrystals exhibited higher degradation efficiencies than did the pure TiO_2 and ZrO_2 samples. Moreover, the stoichiometry of the reactants and the reaction temperature during the synthesis of the nanoparticles affected the photoactivities of these NHSG-derived nanocrystals. The degradation efficiencies increased with increasing Zr-to-Ti ratio. For the samples prepared at 400 °C, we observed the highest photoactivity when the Zr-to-Ti ratio in the $Zr_xTi_{1-x}O_2$ nanocrystals was 0.03. In contrast, the $Zr_xTi_{1-x}O_2$ sample prepared with the same Zr-to-Ti ratio (0.03) but at 320 °C exhibited a lower rate of degradation of RhB. It has been demonstrated that the photoactivities of photocatalysts are mainly related to the amounts of defects. A few defects in a TiO_2 matrix, resulting from the presence of dopants, can play the role of trapping centers to inhibit charge recombination and improve the photoactivity.[24] On the contrary, an excessive number of defects can induce charge recombination and decrease the degree of effective charge. We attribute the highest photoactivity of the $Zr_{0.03}Ti_{0.97}O_2$-400 samples to their moderate content of Zr^{4+} ions in the TiO_2 lattice (Zr-to-Ti ratio of 0.03) and the poor photoactivity of the photocatalysts prepared at low temperature to the great number of surface defects that resulted from the irregular shapes of these particles.

We also compared the photoactivity of the NHSG-derived photocatalysts with that of Degussa P25 TiO_2 in terms of the decoloration of RhB (see Supporting Information, Figure S4). Similarly, the photodecomposition of RhB by Degussa P25 TiO_2 followed pseudo-first-order kinetics, and the pseudo-first-order rate constant (k) was 0.58 min^{-1}. Although Degussa P25 showed a higher apparent photoactivity than the NHSG-derived nanocrystals, the intrinsic photoactivities of the NHSG-derived TiO_2 nanocrystals ($k = 0.02$ g·m^{-2}·min^{-1}) were 1.7 times higher than that of Degussa P25 ($k = 1.2 \times 10^{-2}$ g·m^{-2}·min^{-1}) when normalized to the surface area, because the TOPO-capped TiO_2 (2 m^2/g) has a much smaller specific surface area than Degussa P25 (50 m^2/g). The high intrinsic photoactivities of the NHSG-derived nanocrystals are presumably due to the fact that the surface TOPO enhances the adsorption of RhB onto the photocatalysts.

Conclusions

We have successfully prepared Zr-doped anatase TiO_2 nanorods through the cross-condensation of $Zr/TiCl_4$ with $Zr/Ti(O^iPr)_4$ in anhydrous TOPO at either 320 or 400 °C. The kinetics of the alkyl halide elimination involving the Ti and Zr species plays a crucial role in determining the morphologies, chemical compositions, and crystalline phases of the Zr-doped TiO_2 nanorods. Because the condensation between the Ti species is faster than that between the Zr species, the kinetically controlled reactions cause anatase TiO_2 to be the dominant structure in the nanorods, with the Zr^{4+} ions appearing only as dopants accumulating at the surfaces of the nanocrystals for various initial Zr-to-Ti ratios used in preparation. The existence of less-reactive Zr species in the reaction mixtures retards the nucleation of TiO_2. Therefore, increasing the concentration of Zr species in the precursor solutions increases the sizes of the nanocrystals, and increasing reaction temperatures promote

regular shapes of the nanorods. The photoreactivities of the Zr-doped TiO_2 materials are associated with the amounts of dopants and the shapes of the nanorods. The photocatalysts having the optimal Zr-to-Ti ratio of 0.03 and regular shapes exhibit the highest photoactivities. The TOPO moieties, which we used as capping agents, were chemically bound to the surface of the nanocrystals, either through direct donation of their P=O groups to the surface metal centers or through reformation. The influence of surface TOPO on the mechanisms and dynamics of photocatalysis requires further studies to better understand the photocatalytic chemistry of such surface-modified photocatalysts.

Supporting Information Available: HRTEM images of NHSG-derived TiO_2, ZrO_2, $Zr_{0.05}Ti_{0.95}O_2$-320, and $Zr_{0.67}Ti_{0.33}O_2$-400 nanocrystals; Ti(2p) and Zr(3d) XPS spectra of $Zr_xTi_{1-x}O_2$ nanocrystals; O(1s), P(2p), and C(1s) XPS spectra of NHSG-derived TiO_2 nanocrystals; C-to-O*-to-P molar ratios estimated from the integrated peak areas of the XPS spectra normalized by their atomic sensitivity factors; and photodecomposition of RhB in the presence of Degussa P-25 TiO_2. This material is available free of charge via the Internet at http://pubs.acs.org.

References and Notes

(1) Kabra, K.; Chaudhary, R.; Sawhney, R. L. *Ind. Eng. Chem. Res.* **2004**, *43*, 7683.

(2) Emeline, A. V.; Panasuk, A. V.; Sheremetyeva, N.; Serpone, N. *J. Phys. Chem. B* **2005**, *109*, 2785.

(3) Karunakaran, C.; Senthilvelan, S. *J. Mol. Catal. A: Chem.* **2005**, *233*, 1.

(4) Navio, J. A.; Colon, G.; Macias, M.; SanchezSoto, P. J.; Augugliaro, V.; Palmisano, L. *J. Mol. Catal. A: Chem.* **1996**, *109*, 239.

(5) Sayama, K.; Arakawa, H. *J. Photochem. Photobiol. A* **1996**, *94*, 67.

(6) Schattka, J. H.; Shchukin, D. G.; Jia, J. G.; Antonietti, M.; Caruso, R. A. *Chem. Mater.* **2002**, *14*, 5103.

(7) Chang, S. M.; Doong, R. A. *Chem. Mater.* **2005**, *17*, 4837.

(8) Zhang, Z. B.; Wang, C. C.; Zakaria, R.; Ying, J. Y. *J. Phys. Chem. B* **1998**, *102*, 10871.

(9) Dondi, M.; Matteucci, F.; Cruciani, G. *J. Solid State Chem.* **2006**, *179*, 233.

(10) Shibata, T.; Irie, H.; Ohmori, M.; Nakajima, A.; Watanabe, T.; Hashimoto, K. *Phys. Chem. Chem. Phys.* **2004**, *6*, 1359.

(11) Zhang, Q. H.; Gao, L.; Guo, J. K. *Appl. Catal. B: Environ.* **2000**, *26*, 207.

(12) Vera, C. R.; Pieck, C. L.; Shimizu, K.; Parera, J. M. *Appl. Catal. A: Gen.* **2002**, *230*, 137.

(13) Udompom, A.; Ananta, S. *Mater. Lett.* **2004**, *58*, 1154.

(14) Vioux, A. *Chem. Mater.* **1997**, *9*, 2292.

(15) Andrianainarivelo, M.; Corriu, R.; Leclercq, D.; Mutin, P. H.; Vioux, A. *J. Mater. Chem.* **1996**, *6*, 1665.

(16) Arnal, P.; Corriu, R. J. P.; Leclercq, D.; Mutin, P. H.; Vioux, A. *Chem. Mater.* **1997**, *9*, 694.

(17) Andrianainarivelo, M.; Corriu, R. J. P.; Leclercq, D.; Mutin, P. H.; Vioux, A. *J. Mater. Chem.* **1997**, *7*, 279.

(18) Trentler, T. J.; Denler, T. E.; Bertone, J. F.; Agrawal, A.; Colvin, V. L. *J. Am. Chem. Soc.* **1999**, *121*, 1613.

(19) Joo, J.; Yu, T.; Kim, Y. W.; Park, H. M.; Wu, F. X.; Zhang, J. Z.; Hyeon, T. *J. Am. Chem. Soc.* **2003**, *125*, 6553.

(20) Tang, J.; Fabbri, J.; Robinson, R. D.; Zhu, Y. M.; Herman, I. P.; Steigerwald, M. L.; Brus, L. E. *Chem. Mater.* **2004**, *16*, 1336.

(21) Sham, E. L.; Aranda, M. A. G.; Farfan-Torres, E. M.; Gottifredi, J. C.; Martinez-Lara, M.; Bruque, S. *J. Solid State Chem.* **1998**, *139*, 225.

(22) Yang, J.; Ferreira, J. M. F. *Mater. Res. Bull.* **1998**, *33*, 389.

(23) Emeline, A.; Kataeva, G. V.; Litke, A. S.; Rudakova, A. V.; Ryabchuk, V. K.; Serpone, N. *Langmuir* **1998**, *14*, 5011.

(24) Choi, W. Y.; Termin, A.; Hoffmann, M. R. *J. Phys. Chem.* **1994**, *98*, 13669.